MATER. RES. LETT.
2024, VOL. 12, NO. 3, 180–189
https://doi.org/10.1080/21663831.2024.2312146

MATERIALS RESEARCH LETTERS
Taylor & Francis
Taylor & Francis Group

ORIGINAL REPORTS

OPEN ACCESS  Check for updates

# Recovery facilitated by interphase boundary motion circumvents recrystallization in superalloy single crystals

Hongfei Zhang[a], Kai Chen [a], Sicong Lin[a], Rui Fu[b], Bozhao Zhang[a], Jun Ding[a], Zongqiang Feng[b], Xiaoxu Huang [b] and Evan Ma[a]

[a]State Key Laboratory for Mechanical Behavior of Materials, Xi'an Jiaotong University, Xi'an, People's Republic of China; [b]International Joint Laboratory for Light Alloys (MOE), College of Materials Science and Engineering, Chongqing University, Chongqing, People's Republic of China

**ABSTRACT**
Dislocation recovery lowering the driving force for recrystallization would be able to suppress the latter in Ni-based superalloy single crystals, but was believed unlikely due to their low stacking-fault energy. Defying this traditional wisdom, here we show that efficient recovery can be realized once the $\gamma'$-precipitates start to dissolve. Our microscopy evidence tracking the distribution/configuration of dislocations reveals that the shifting $\gamma/\gamma'$ interphase boundaries release the dislocations trapped there, facilitating their annihilation and rearrangement into low-energy network configurations. Our finding explains the success of a recent recovery protocol that kept superalloys as single crystals after supersolvus homogenization heat treatment.

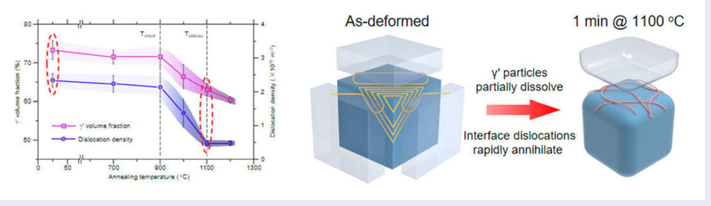


**IMPACT STATEMENT**
In $\gamma/\gamma'$ two-phase Ni-based superalloy single crystals, dislocation recovery is achieved via an interphase-boundary motion enabled mechanism, defying the traditional wisdom of dislocation climb/cross-slip controlled by stacking-fault energy.

**ARTICLE HISTORY**
Received 6 November 2023

**KEYWORDS**
Dislocation recovery; interphase-boundary motion; Ni-based superalloy single crystals; TEM tomography

## 1. Introduction

Ni-based superalloys are the materials of choice to manufacture turbine components in aerospace and power generation industries [1]. Their superior properties rely on the large volume fraction of strengthening $\gamma'$-particles embedded in the solid-solution $\gamma$-framework [2,3]. To further improve their creep resistance, superalloy single crystals with no high-angle grain boundaries have been developed [4]. However, manufacturing with significant shape changes via solidification and machining inevitably involves plastic strains mediated by dislocations, and post-manufacturing heat treatment easily triggers recrystallization [5–7]. Although annealing the single crystals at temperatures well below the $\gamma'$-solvus point would reduce the risk of recrystallization, it is not an option because such a treatment leaves unacceptable chemical/microstructure inhomogeneities [8,9]; industrial standard heat treatment protocols therefore require homogenization-annealing at supersolvus temperatures. This makes it very challenging to keep the pre-strained single crystals from recrystallization.

Recrystallization has long been considered unpreventable in supersolvus heat-treated superalloys [6,7,10] once the plastic strain they experienced exceeds a critical threshold strain of only 1-2% [5–7]. A comprehensive summary of the previous publications on preventing recrystallization in superalloy single crystals deformed at room-temperature can be found in Supplementary

**CONTACT** Kai Chen kchenlbl@gmail.com State Key Laboratory for Mechanical Behavior of Materials, Xi'an Jiaotong University, Xi'an, Shaanxi 710049, People's Republic of China; Xiaoxu Huang xiaoxuhuang@cqu.edu.cn International Joint Laboratory for Light Alloys (MOE), College of Materials Science and Engineering, Chongqing University, Chongqing 400044, People's Republic of China; Evan Ma maen@xjtu.edu.cn State Key Laboratory for Mechanical Behavior of Materials, Xi'an Jiaotong University, Xi'an, Shaanxi 710049, People's Republic of China

Supplemental data for this article can be accessed online at https://doi.org/10.1080/21663831.2024.2312146.

Table 1. In those cases, recrystallization was not avoided successfully at higher plastic strains because the recovery annealing temperature was either rather low ($\sim$0.5 homologous temperature or lower, as for single-phase alloys) or too high (solvus temperature or higher, which triggered recrystallization). The poor recovery capabilities of superalloys were ascribed to their low stacking-fault energy [11,12] (SFE, about 20–30 mJ/m$^2$) [13–15]. However, such attention to SFE, while appropriate to understand the recovery/recrystallization behaviors of single-phase materials, is nevertheless inadequate for two-phase alloys as complex as superalloys, which, unlike alloys dispersed with low volume fractions (usually no more than 5%) of precipitates, contain abundant (volume fraction up to 70%) $\gamma'$-particles [16–19]. Because of the influence of the high-volume fractions of the strengthening precipitates, the dislocation microstructures in the deformed superalloys become more complicated and harder to characterize. Therefore, significant discrepancies and even contradictions have been reported on the dislocation distribution and configuration in the literature. a detailed summary of which can be found in Supplementary Table 2. For room-temperature deformed superalloys, some demonstrated [20–22] transmission electron microscope (TEM) images of straight dislocations aligned in $\gamma$-channels, while others believed that [23,24] those parallel lines were superpartial dislocation pairs separated by planar defects, evidencing that high densities of dislocations had cut into the $\gamma'$-particles. Moreover, since the previous investigations continued to follow the ideas for recovery/recrystallization of single-phase materials, they focused on SFEs rather than on dislocation-precipitate interactions.

Recrystallization renders the microstructure polycrystalline, which would forfeit the single-crystal benefits and significantly degrade the high-temperature creep performance of superalloys [4]. Thus, recrystallization has been a formidable obstacle for the manufacturing and application of Ni-based superalloy single crystals. In this study, advanced TEM tomography is applied to directly track the distribution of dislocations and their configurations in the as-deformed state and then their annihilation during annealing. Based on the understanding of the interplay between the dislocations and precipitates, in particular the role played by the interface boundaries, we demonstrate when and how recrystallization can be completely pre-empted by a recovery annealing. The latter has been optimized to as short as 30 min, which is significant for the manufacturing and repair of superalloys. Our discovery reveals that the recovery mechanism in the two-phase superalloys defies the conventional knowledge for single-phase alloys.

## 2. Materials and methods

The AM3 superalloy single-crystalline boule (chemical composition is shown in Supplementary Table 3) growing along [001] direction was machined into cylindrical (5 mm in diameter and 10 mm in height) specimens for compression tests at room-temperature at a constant strain rate of $1.69 \times 10^{-4}$ s$^{-1}$. The plastic strain, 4.5% in this work, was measured from the height reduction of the deformed cylinders. The deformed cylinders were sliced perpendicular to the [001] direction into 1-mm-thick discs for heat treatment investigations. More information can be found in Supplementary Figure 1 and Note 1.

The as-deformed and heat-treated samples were characterized using scanning electron microscope (SEM), electron backscattered diffraction (EBSD), TEM, and synchrotron radiation micro-Laue diffraction (SR-$\mu$Laue) techniques. The deformation microstructure characterizations were carried out on samples taken from the interior of the bulk superalloys, and the absence of recrystallization was confirmed both on the surface and in the bulk. TEM thin foils were made from the strain-concentrated areas, and then ten bright-field images were collected for each deformation or annealing state to improve reproducibility, all along the [001] zone axis. Subsequently, the dislocation density was measured from each image using the line-intercept method [25] and averaged. TEM tomography was performed on a FEI TECNAI G20 TEM operated at 200 kV. To optimize the contrast of dislocations, g = $[\bar{2}20]$ and g = $[2\bar{2}0]$ two-beam conditions were selected to acquire a series of weak-beam dark-field images from $-47^{\circ}$ to $44^{\circ}$ and $-55^{\circ}$ to $66^{\circ}$ for deformed and 1 min-annealed at 1100 °C specimens, respectively, with an angular step of $1^{\circ}$. More details can be found in Supplementary Note 1.

## 3. Results

The residual lattice strain and misorientation distributions in the 4.5% room-temperature compressed superalloy single crystal, mapped using the SR-$\mu$Laue method, are highly non-uniform. Von Mises strains near the deformation concentrated regions (indicated by blue arrows in Figure 1a), especially at their intersections, reach up to $50 \times 10^{-3}$, almost two orders of magnitude higher than the average, proving severe lattice distortions and hence concentrated strain energy in the narrow zones. Along the deformation concentrated zones, low-angle misorientations are also detected (Figure 1b), up to $1^{\circ}$. As highlighted by the dashed orange lines in the bright-field TEM image of the deformation concentrated region in Figure 1c, the cuboidal $\gamma'$-particles

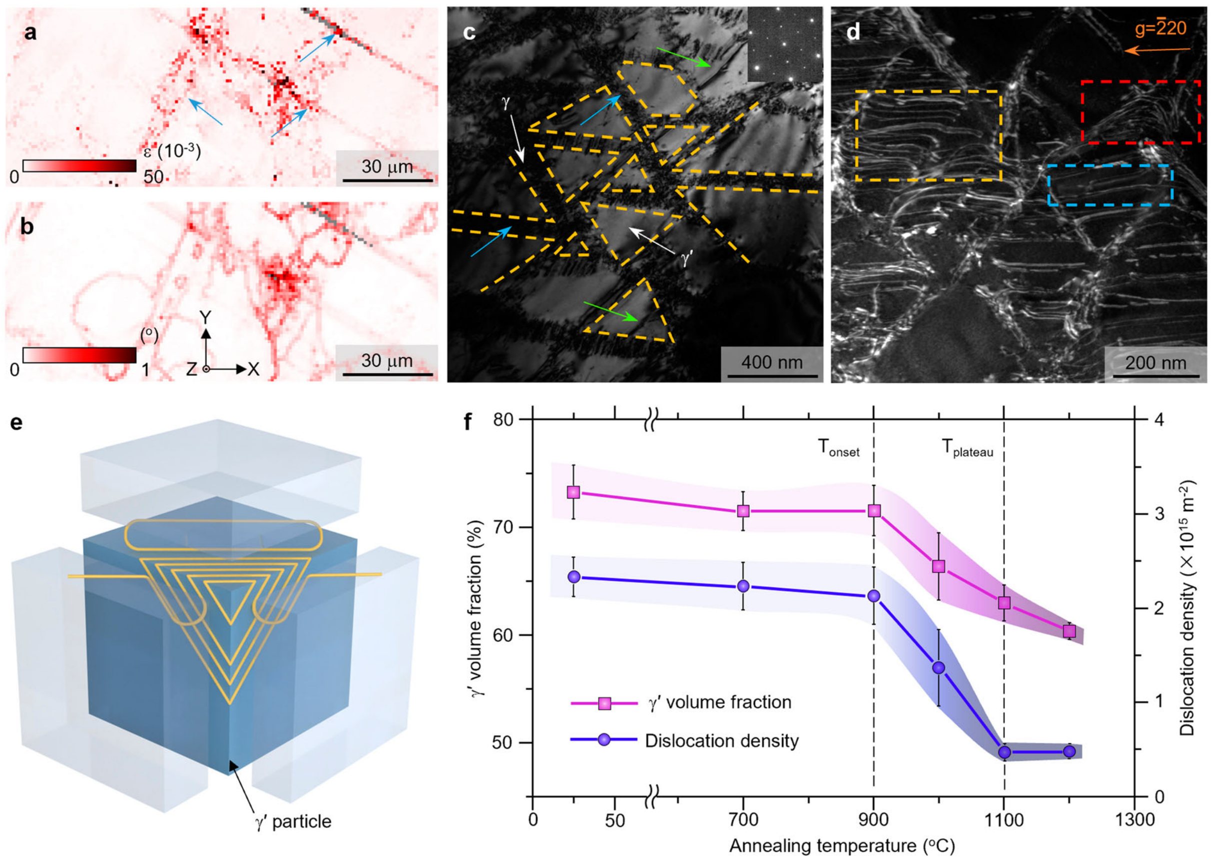


**Figure 1.** The microstructures in the superalloy single crystal compressed in the [001] direction. (a) Von Mises strain map, showing the elastic strain associated with the accumulated dislocations. (b) Kernel average misorientation map. (c) Bright-field TEM image of the deformed sample observed in [111] crystallographic direction. (d) Snapshot from the dark-field tomography video of the deformed sample. (e) The schematic of dislocations in the deformed sample. (f) The $\gamma'$ volume fraction and dislocation density after annealing at elevated temperatures (the width of the bands corresponds to the measurement error, and the vertical dash lines indicate the onset and plateauing temperatures of the dislocation density drop), showing a strong coupling between the $\gamma'$ dissolution and accelerated dislocation density decrease.

projected onto the (111) crystallographic plane appear as triangles and hexagons surrounded by narrow $\gamma$-channels, into which most of dislocations are jammed (indicated by the blue arrows). Only a small number of dislocations are detected cutting into the $\gamma'$-particles (pointed using green arrows). Along various zone axes, those dislocations in $\gamma$-channels are straight and aligned in $<110>$ crystallographic directions (Supplementary Figure 2). Exploiting TEM tomography (Figure 1d, as well as in Supplementary Figure 3), the morphology and spatial distribution of the dislocations in the $\gamma$-channels can be better visualized. Dislocation loops, either residing in a certain $\gamma$-channel [20,21] (those in the blue box) or surrounding a $\gamma'$-particle [26] (those in the red box), are commonly observed. Some other dislocations have partially bowed out of its original $\gamma$-channel and extruded into the perpendicular ones [26,27] (yellow box). Based on the TEM observations, the dislocation configurations are schematically displayed in Figure 1e.

The dislocation density in the deformation concentrated regions is measured to be $2.3 \times 10^{15}$ m$^{-2}$. Based on detailed analysis under different two-beam conditions (Supplementary Figure 4 and Note 2), the Burgers vector of most of the dislocations are determined to be $\pm\frac{a}{2}[101]$ for the locations analyzed here.

To investigate the recovery and the associated dislocation behavior, the deformed single crystal was annealed at various temperatures for nominally 1 min each (as schematically shown in Supplementary Figure 1c). As clearly seen in Figure 1f, the dislocation density drop and $\gamma'$ partial dissolution are strongly coupled. The dislocations are by and large recovered (by $\sim 80\%$) after being annealed at 1100 °C for only 1 min. More detailed analysis will be described in Figure 2.

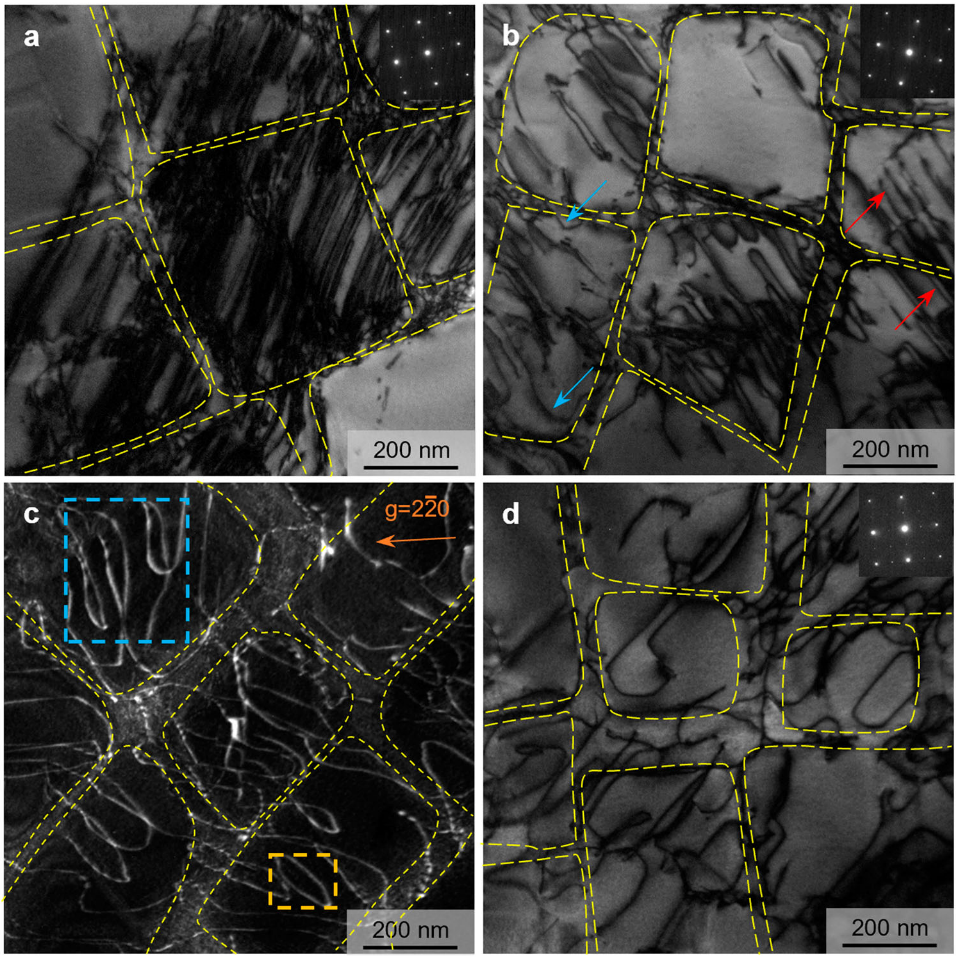


**Figure 2.** Dislocation structure after the one-minute annealing at (a) 900 °C, (b) 1000 °C, (c) 1100 °C and (d) 1200 °C.

Annealing at temperatures below 900 °C is not able to induce any significant change in terms of both the $\gamma'$ volume fraction/morphology and the dislocation density/configuration (Figure 2a). Above 900 °C, the volume fractions of primary $\gamma'$-precipitates keeps decreasing with increasing temperature. Along with this subsolvus solutionizing, the density of left-over dislocations drops monotonically with increasing temperature. After annealing at 1000 °C (Figure 1f and Figure 2b), about 30% of the dislocations are annihilated. Some left-over dislocations become curly (blue arrows), while some still keep their original straight shape (red arrows). When the temperature is elevated to 1100 °C, more than 80% dislocations are annealed out, leaving a low density of only $4.7 \times 10^{14}$ $m^{-2}$ (Figure 1f). Detailed TEM tomography analysis (Figure 2c, as well as in Supplementary Figure 5) proves that almost all the remaining dislocations are still lying in $\gamma$-channels, but become well separated from one another. In the field of view, all dislocations turn highly curly (blue box), or even shrink into small loops (yellow box), with few straight ones left. Despite the significant morphology and density evolution, the Burgers vector of the left dislocations remains unchanged (Supplementary Figure 6 and Note 2). As the annealing temperature is further elevated (to 1200 °C for example), although the $\gamma'$ volume fraction keeps decreasing, no further significant change is observed in terms of dislocation density and configuration, compared to the 1100 °C annealed specimen (Figure 2d).

The key observation above is that the onset temperature ($T_{onset}$) of dislocation recovery above which accelerated dislocation annihilation can be realized is the same as the one that $\gamma'$-particle starts to dissolve (900 °C in this case). Moreover, from the plot in Figure 2a, another characteristic temperature, the plateau temperature ($T_{plateau}$), is also figured out, at which the dislocation annihilation rate is maximum (1100 °C in this case).

In order to achieve a more complete relief of the stored elastic strain energy, we design a stepped recovery heat treatment as shown in Figure 3a. The recovery takes 30 min in total, which is less than 1/20 compared to the previously reported long term/cyclic protocol [6], and 1/4 of our own former study [22]. After

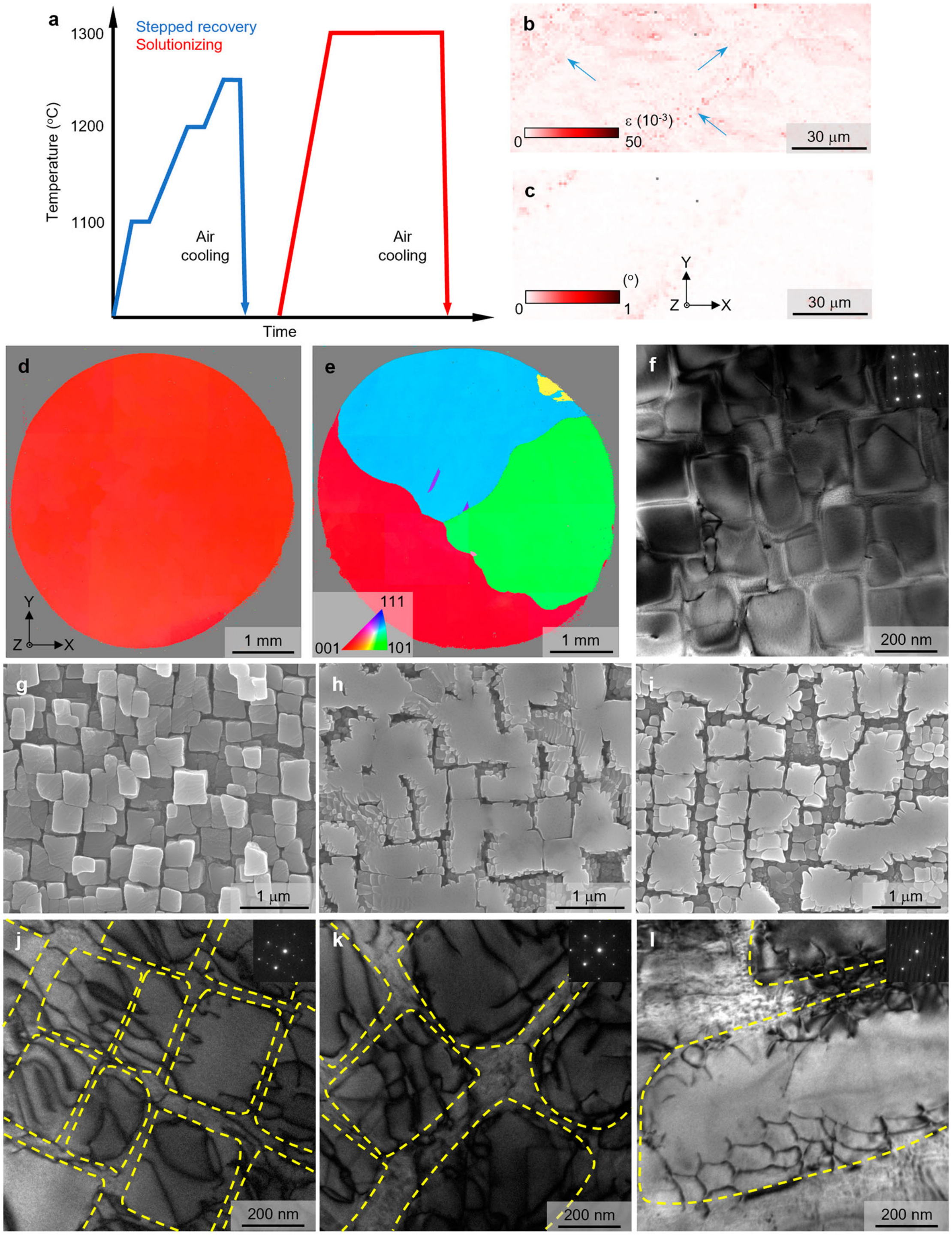


**Figure 3.** Thorough recovery of the 4.5% plastically deformed superalloy single crystal. (a) The schematic of stepped recovery strategy and solutionizing heat treatment (details in Supplementary Note 1). The von Mises strain map (b) and the KAM map (c) of the fully recovered single crystal. The IPF-Z figure of the supersolvus solutionizing heat-treated superalloys (d) with and (e) without recovery annealing. (f) Bright-field TEM image of stepped recovered and solutionized sample. The evolution of $\gamma'$-particles and dislocation interrupted the rapid stepwise recovery heat treatment at (g, j) 1100 °C, (h, k) 1200 °C, and (i, l) 1250 °C, respectively.

such short recovery, although the deformation concentrated regions are still detectable (blue arrows in Figure 3b), much lower and more homogeneous residual strains and misorientations are measured around them (Figure 3b,c), indicating effectively diminished driving force for recrystallization. After the stepped recovery, a supersolvus treatment is conducted at 1300 °C for 30 min, which is much longer than that previously found for the recrystallizing grains — if any — to nucleate and grow [28,29]. Yet, EBSD scan over the entire sample surface evidences the single crystalline structure and excludes the existence of recrystallized grains (Figure 3d). In contrast, recrystallized grains readily form at 1300 °C without recovery (Figure 3e). After recovery and supersolvus treatment, dislocations can be hardly detected (Figure 3f).

The microstructure evolution during the stepped recovery treatment is studied in detail. With the temperature increasing and the holding time prolonging, $\gamma'$-particles in the deformation concentrated zones gradually evolve from the cuboidal shape (Figure 3g) to the rafts (Figure 3h) and eventually to the butterfly shape (Figure 3i). Since the $\gamma'$-particles dissolution rate is higher along the dislocation pipes, grooves are generated on the $\gamma'$-particles [30]. The coarsening directions observed in the $\gamma'$-precipitates displayed in Figure 3h,i are non-uniform, because of the locally inhomogeneous stresses in these deformation concentrated zones (Supplementary Figure 7b and 7d). In the meantime, the curly dislocations (Figure 3j) begin to react with each other (Figure 3k) and finally form regular hexagonal dislocation networks at $\gamma/\gamma'$ interface (Figure 3l, as well as in Supplementary Figure 8), a low-energy dislocation configuration [31,32], which result the stored energy further decreasing.

## 4. Discussion

First of all, SFE is known to be a key factor influencing dislocation recovery [16]. Previous studies [13–15] show that the SFE of $\gamma$-matrix in superalloy single crystals is only 20–30 mJ/m$^2$, which drives the dislocations to dissolve into immobile partials that are unwilling to cross-slip and climb to annihilate, assuming the SFE keeps almost constant as the temperature increases [15]. However, in the current study, the observed rapid dislocation annihilation at 1100 °C suggests that the SFE of the $\gamma$-matrix is not low near the $\gamma'$-solvus temperature. To demonstrate that this is the case, we performed molecular dynamics simulations for two different states of the $\gamma$-matrix (details in Supplementary Note 3): (1) the $\gamma$-phase is assumed to be a completely random solid-solution, (2) chemical short-range order is taken into consideration. As shown in Figure 4a, the calculated SFE at room-temperature, 25–45 mJ/m$^2$, is consistent with the literature reports [13–15]. But the SFE increases at elevated temperatures. At 1100 °C, the SFE increases to about 62 mJ/m$^2$ (random solution) and over 80 mJ/m$^2$ (due to chemical short-range order), which are much higher than those of the easy-to-recrystallize metals such as Ag ($\sim$20 mJ/m$^2$) [33,34] and austenitic stainless steel ($\sim$20 mJ/m$^2$) [35,36]. Therefore, dislocation splitting into partials with wide separation distance, which would retard the dislocations movement and hence annihilation, is not the key factor of recovery at elevated temperatures.

More importantly, by comparing the normalized dislocation density in pre-strained superalloy AM3 (this work) with deformed commercially pure aluminum (high SFE) [37] and austenite stainless steel (low SFE) [38] in Figure 4b, we can clearly see the difference in the recovery and recrystallization behaviors. Single-phase alloys, no matter the SFE is high or low, would first exhibit recovery (RV, displayed as solid blue and green curves) and then recrystallization (RX, shown as dashed curves) as the annealing temperature increases. Although the high SFE alloys show more recovery capabilities than the low SFE alloys, the recovery induced dislocation density decrease in both cases is less than 20%, because, according to the classic recovery theory, point defects will be activated and annihilated prior to the dislocations. A precipitous decrease in dislocation density sets in only upon recrystallization (dashed curves). However, in the two-phase superalloys, a barely detectable recovery stage is followed by a drastically accelerated recovery stage, which leads to a (almost abrupt) drop in dislocation density by 80% or more and a complete prevention of recrystallization at high homologous temperatures. This leads to an unusual recovery behavior: 'solid curve all the way, eliminating the dashed curve' (see Figure 4b).

The above unusual dislocation recovery behavior of superalloy single crystals is rooted in their two-phase microstructure and deformation mechanism. Through TEM tomography, the spatial distribution, configuration, and Burgers vectors of dislocations can be unequivocal characterized. The dislocations originate and multiply in single $\gamma$-channels at the beginning of the room-temperature plastic deformation. As strain increases, dislocations move in the $\gamma$-channels until being stopped by the $\gamma'$-particles. To carry more deformation, some dislocations have to bow-out into the perpendicular $\gamma$-channels, following the Orowan bypass mechanism [21], because the stress is not high enough to drive the dislocations to cut into $\gamma'$-particles. As the bow-out process goes further, dislocation loops surrounding $\gamma'$-particles are eventually generated. Due to the coherency strain, numerous dislocations are trapped at the $\gamma/\gamma'$ interfaces. This is why the onset of dislocation recovery is coincident with the partial dissolution of $\gamma'$. Partial dissolution implies adequate atomic diffusion and entails a mobile $\gamma/\gamma'$ interface, creating opportunities for the previously stuck dislocations to move around and interact with each other in less than several minutes. Regretfully, the kinetics of dislocation motion and reaction are difficult to observe during in-situ heating experiment in

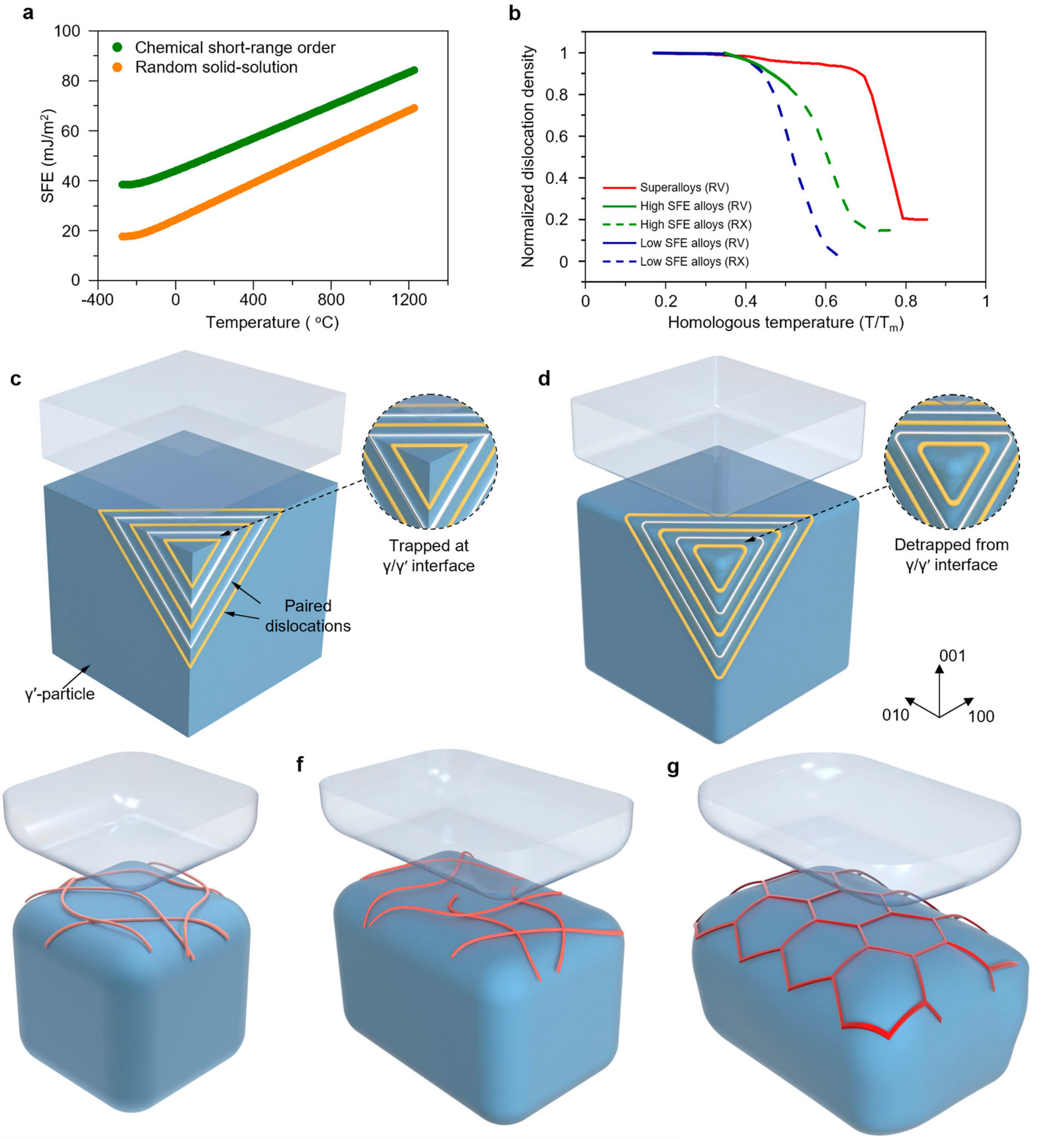


**Figure 4.** (a) Temperature-dependent SFE of the $\gamma$-phase under the random solid-solution and chemical short-range order conditions, from molecular dynamics simulations. (b) Schematic showing dislocation density as a function of annealing temperature in recovery/recrystallization (RV/RX), comparing our pre-strained two-phase superalloy with single-phase alloys with either high (commercially pure aluminum [37]) or low (austenite stainless steel [38]) stacking-fault energies. (c-g) Schematics showing the (c) trapping, (d) detrapping, (e) annihilation and climbing/cross-slip, (f) irregular network, and (g) hexagonal network formation of the dislocations in the vicinity of the $\gamma/\gamma'$ interface.

TEM, because for TEM observations the specimens have to be thinned down to less than 100 nm, which is only a quarter of the size of typical $\gamma'$-particles, and the dislocations would be easily annealed out from the sample surfaces, before interacting with $\gamma/\gamma'$ interfaces.

It is known that the driving force of recrystallization, $P$, is the product of the dislocation density, $\rho$, and the energy per unit length of dislocation line, $E_{dis}$ [39],

$$P = \Delta(\rho \cdot E_{dis}) \quad (1)$$

For the 4.5% deformed AM3, with merely one-minute annealing at 1100 °C, the density of dislocations drops dramatically by a factor of 5. What is more, the remaining dislocations turn curly due to the cross-slip or climb, suggesting configurational evolution that lowers the energy per unit length. As a result, $P$ is reduced to less than 20% of the deformed state. Less dislocations are annihilated at 1000 °C than at 1100 °C because at the lower temperature some dislocations are still not let go by the $\gamma/\gamma'$ interface. 1200 °C does not annihilate more dislocations than 1100 °C, indicating that at 1100 °C, $\gamma'$-particle has dissolved enough such that all dislocations trapped by the interphase boundaries have become mobile. The annihilated dislocations (accounting for 80%) must have been paired ones with opposite Burgers vector ($\pm\frac{\boldsymbol{a}}{2}[101]$), and the spacing between each paired dislocations is only several nanometers (shown in Figure 1d), which makes the annihilation so rapid (Figure 4c,d). The remnant 20% are unpaired such that their density keeps almost constant even at higher temperatures and longer annealing times. However, they find their own way to lowering the stored strain energy by changing configurations, including climbing or cross-slip to become curly (Figure 4e), interacting with each other to form irregular dislocation networks (Figure 4f), and gradually rearranging into low-energy hexagonal dislocation networks (Figure 4g). According to the classic theory [39], the energy per unit length of dislocation is consisted of self-energy and interaction-energy. The self-energy is material and temperature dependent, while the interaction-energy depends strongly on the configuration of dislocations. Dislocation reconfiguration and rearrangements reduces the interaction-energy. As a result, the energy associated with the dislocations, and thus the driving force for recrystallization, is further reduced.

Finally, we compare our current recovery protocol with the previously reported ones. In many of the previous investigations, recovery annealing was either too low to reduce recrystallization driving force [7], or too high to trigger recrystallization directly [11]. In this study, two critical temperatures, $T_{onset}$ and $T_{plateau}$, are marked (Figure 1f). Recovery annealing is better carried out from some point between these two temperatures to be efficient and safe. Our own successful experience obeyed this rule [22], and thus recrystallization is completely pre-empted even with 5.9% room-temperature plastic strain. However, we must admit that our previous heat treatment protocol, because of the unknown recovery mechanism and kinetics, was rather conservative, but not the most efficient in time and energy. In the current study, we not only optimized the recovery annealing protocol (from previous 2 h to current 30 min) for room-temperature compressed AM3, but also revealed the dislocation evolution stages (with two critical temperatures, $T_{onset}$ and $T_{plateau}$) using a state-of-the-art TEM methodology to figure out why the innovated protocol can circumvent recrystallization in superalloys.

## 5. Conclusion

In sum, through TEM tomography, we confirm that with about 4.5% plastic strain in superalloy single crystals, dislocations are generated and multiplicated in the $\gamma$-channels, but almost impossible to cut into the $\gamma'$ particles, leading to numerous dislocations pinned at the $\gamma/\gamma'$ interfaces. Due to such microstructural features, annihilation of dislocations cannot be achieved unless the annealing temperature is above $T_{onset}$, to dissolve the $\gamma'$-particles partially such that the $\gamma/\gamma'$ interfaces are set in motion to liberate the stuck dislocations. Systematic investigation suggests 1100 °C ($T_{plateau}$) as an optimized temperature to have dislocations annihilated thoroughly with little risk of recrystallization. Short annealing reduces the driving force for recrystallization by more than 80%. What is more, with prolonged annealing time above $T_{plateau}$, dislocations keep evolving into lower-energy networks, further diminishing the driving force for recrystallization. Based on these findings, an efficient and inexpensive (only half an hour) heat treatment protocol has been established for superalloy single crystals to completely avoid recrystallization during supersolvus homogenization heat treatment. Therefore, our study offers an efficient way to lower the rejection rate and thus the overall cost of superalloy single crystal blades. In terms of advances in materials science, we have discovered a new recovery-controlling mechanism for high-volume fraction multiphase alloys, for which the interphase-boundary-detrapping becomes the rate-limiting step, in lieu of the traditional dislocation climb/cross-slip processes. This leads to unusual consequences as depicted in Figure 4b, where the normal recovery of dislocations with increasing temperature, well known to be gradual until recrystallization, is replaced by a wide 'hold before burst' regime up to a threshold temperature at which a precipitous drop kicks in (red curve), to the level that the recrystallization can be pre-empted altogether.

## Acknowledgements

We thank Instrumental Analysis Center of Xi'an Jiaotong University and Dr. Chuanwei Fan from CAMPNano for technical support.

## Disclosure statement

No potential conflict of interest was reported by the author(s).

## Funding

This work was supported by National Science and Technology Major Project: [Grant Number 2019-VII-0019-0161]; National Key Research and Development Program of China: [Grant Number 2023YFB3712002]; National Natural Science Foundation of China: [Grant Number 51927801, U2032205, and 52271042]; 111 Project 2.0: [Grant Number BP0618008].

## ORCID

*Kai Chen* http://orcid.org/0000-0002-4917-4445
*Xiaoxu Huang* http://orcid.org/0000-0002-4635-6112

## References

[1] Reed RC. The superalloys: fundamentals and applications. Cambridge: Cambridge University Press; 2008.
[2] Pollock TM, Tin S. Nickel-based superalloys for advanced turbine engines: chemistry, microstructure and properties. J Propul Power. 2006;22:361–374. doi:10.2514/1.18239
[3] Pollock TM. Alloy design for aircraft engines. Nature Mater. 2016;15:809–815. doi:10.1038/nmat4709
[4] Koff BL. Gas turbine technology evolution: a designers perspective. J Propul Power. 2004;20:577–595. doi:10.2514/1.4361
[5] Bond S, Martin J. Surface recrystallization in a single crystal nickel-based superalloy. J Mater Sci. 1984;19:3867–3872. doi:10.1007/BF00980749
[6] Bürgel R, Portella P, Preuhs J. Recrystallization in single crystals of nickel base superalloys. Superalloys. 2000;5:229–238.
[7] Cox D, Roebuck B, Rae C, et al. Recrystallisation of single crystal superalloy CMSX–4. Mater Sci Technol. 2003;19:440–446. doi:10.1179/026708303225010731
[8] Rettberg L, Callahan P, Goodlet B, et al. Rejuvenation of directionally solidified and single-crystal Nickel-base superalloys. Metall Mater Trans A. 2021;52:1609–1631. doi:10.1007/s11661-021-06150-7
[9] Lin S, Chen K, He W, et al. Custom-designed heat treatment simultaneously resolves multiple challenges facing 3D-printed single-crystal superalloys. Mater Des. 2022;222:111075), doi:10.1016/j.matdes.2022.111075
[10] Panwisawas C, Mathur H, Gebelin JC, et al. Prediction of recrystallization in investment cast single-crystal superalloys. Acta Mater. 2013;61:51–66. doi:10.1016/j.actamat.2012.09.013
[11] Li Z, Xu Q, Liu B. Microstructure simulation on recrystallization of an as-cast nickel based single crystal superalloy. Comput Mater Sci. 2015;107:122–133. doi:10.1016/j.commatsci.2015.05.020
[12] Li Z, Fan X, Xu Q, et al. Influence of deformation temperature on recrystallization in a Ni-based single crystal superalloy. Mater Lett. 2015;160:318–322. doi:10.1016/j.matlet.2015.07.120
[13] Benyoucef M, Décamps B, Coujou A, et al. Stacking-fault energy at room temperature of the $\gamma$ matrix of the MC2 Ni-based superalloy. Philos Mag A. 1995;71:907–923. doi:10.1080/01418619508236228
[14] Décamps B, Morton AJ, Condat M. On the mechanism of shear of $\gamma'$ precipitates by single (a/2)⟨110⟩dissociated matrix dislocations in Ni-based superalloys. Philos Mag A. 1991;64:641–668. doi:10.1080/01418619108204866
[15] Pettinari F, Douin J, Saada G, et al. Stacking fault energy in short-range ordered $\gamma$-phases of Ni-based superalloys. Mater Sci Eng A. 2002;325:511–519. doi:10.1016/S0921-5093(01)01765-8
[16] Humphreys FJ, Hatherly M. Recrystallization and related annealing phenomena. New York: Elsevier; 2012.
[17] Doherty RD, Hughes DA, Humphreys FJ, et al. Current issues in recrystallization: a review. Mater Sci Eng A. 1997;238:219–274. doi:10.1016/S0921-5093(97)00424-3
[18] Raabe D. Recovery and recrystallization: phenomena, physics, models, simulation. In: DE Laughlin, K Hono, editor. Physical metallurgy, fifth ed. Elsevier; 2014. p. 2291–2397.
[19] Huang K, Marthinsen K, Zhao Q, et al. The double-edge effect of second-phase particles on the recrystallization behaviour and associated mechanical properties of metallic materials. Prog Mater Sci. 2018;92:284–359. doi:10.1016/j.pmatsci.2017.10.004
[20] Luo Z, Wu Z, Miller D. The dislocation microstructure of a nickel-base single-crystal superalloy after tensile fracture. Mater Sci Eng A. 2003;354:358–368. doi:10.1016/S0921-5093(03)00039-X
[21] Kubin L, Lisiecki B, Caron P. Octahedral slip instabilities in $\gamma/\gamma$' superalloy single crystals CMSX-2 and AM3. Philos Mag A. 1995;71:991–1009. doi:10.1080/01418619508236233
[22] Lin S, Chen K, Zeng Q, et al. A method for increasing the supersolvus critical strain for recrystallization in single-crystal superalloys. Mater Res Lett. 2023;11:856–862. doi:10.1080/21663831.2023.2253267
[23] Milligan W, Antolovich S. Yielding and deformation behavior of the single crystal superalloy PWA 1480. Metall Trans A. 1987;18:85–95. doi:10.1007/BF02646225
[24] Feller-Kniepmeier M, Link T, Poschmann I, et al. Temperature dependence of deformation mechanisms in a single crystal nickel-base alloy with high volume fraction of $\gamma'$ phase. Acta Mater. 1996;44:2397–2407. doi:10.1016/1359-6454(95)00354-1
[25] Norfleet D, Dimiduk D, Polasik S, et al. Dislocation structures and their relationship to strength in deformed nickel microcrystals. Acta Mater. 2008;56:2988–3001. doi:10.1016/j.actamat.2008.02.046
[26] Tinga T, Brekelmans WAM, Geers MGD. Cube slip and non-Schmid effects in single crystal Ni-base superalloys. Model Simul Mater Sci Eng. 2010;18:015005), doi:10.1088/0965-0393/18/1/015005
[27] Benyoucef M, Clement N, Coujou A. Transmission electron microscope in situ deformation of MC2 superalloy at room temperature. Mater Sci Eng A. 1993;164:401–406. doi:10.1016/0921-5093(93)90701-F
[28] Mathur HN, Panwisawas C, Jones CN, et al. Nucleation of recrystallisation in castings of single crystal Ni-based superalloys. Acta Mater. 2017;129:112–123. doi:10.1016/j.actamat.2017.02.058
[29] Chen K, Huang R, Li Y, et al. Rafting-enabled recovery avoids recrystallization in 3D-printing-repaired single-crystal superalloys. Adv Mater. 2020;32:1907164), doi:10.1002/adma.201907164

[30] Parsa AB, Wollgramm P, Buck H, et al. Ledges and grooves at $\gamma/\gamma'$ interfaces of single crystal superalloys. Acta Mater. 2015;90:105–117. doi:10.1016/j.actamat.2015.02.005

[31] Kuhlmann-Wilsdorf D. LEDS: Properties and effects of low energy dislocation structures. Mater Sci Eng. 1987;86:53–66. doi:10.1016/0025-5416(87)90442-3

[32] He J, Cao L, Makineni SK, et al. Effect of interface dislocations on mass flow during high temperature and low stress creep of single crystal Ni-base superalloys. Scr Mater. 2021;191:23–28. doi:10.1016/j.scriptamat.2020.09.016

[33] Gallagher P. The influence of alloying, temperature, and related effects on the stacking fault energy. Metall Trans. 1970;1:2429–2461. doi:10.1007/BF03038370

[34] Kibey S, Liu J, Johnson DD, et al. Predicting twinning stress in fcc metals: Linking twin-energy pathways to twin nucleation. Acta Mater. 2007;55:6843–6851. doi:10.1016/j.actamat.2007.08.042

[35] Schramm RE, Reed RP. Stacking fault energies of seven commercial austenitic stainless steels. Metall Trans A. 1975;6:1345–1351. doi:10.1007/BF02641927

[36] Lu J, Hultman L, Holmström E, et al. Stacking fault energies in austenitic stainless steels. Acta Mater. 2016;111: 39–46. doi:10.1016/j.actamat.2016.03.042

[37] Alyani A, Kazeminezhad M. Annealing behavior of aluminum after low-temperature severe plastic deformation. Mater Sci Eng A. 2021;824:141810), doi:10.1016/j.msea.2021.141810

[38] Shakhova I, Dudko V, Belyakov A, et al. Effect of large strain cold rolling and subsequent annealing on microstructure and mechanical properties of an austenitic stainless steel. Mater Sci Eng A. 2012;545:176–186. doi:10.1016/j.msea.2012.02.101

[39] Bailey J, Hirsch P. The dislocation distribution, flow stress, and stored energy in cold-worked polycrystalline silver. Philos Mag. 1960;5:485–497. doi:10.1080/14786436008238300